Laser powder bed fusion of a nanocrystalline Finemet Fe-based alloy for soft magnetic applications ⓕ

Special Collection: Laser Manufacturing for Future Mobility

S. Sadanand ⓘ ; M. Rodríguez-Sánchez ⓘ ; A. Ghavimi ⓘ ; R. Busch ⓘ ; P. Sharangi; P. M. Tiberto ⓘ ;
E. Ferrara ⓘ ; G. Barrera ⓘ ; L. Thorsson ⓘ ; H. J. Wachter ⓘ ; I. Gallino ⓘ ; M. T. Pérez-Prado ✉ ⓘ

Check for updates

View Online   Export Citation

Articles You May Be Interested In

Magnetostriction and effective magnetic anisotropy of Co-contained Finemet nanocrystalline alloys

J. Appl. Phys. (April 2010)

Microstructure and magnetic properties of FINEMET nanowires

J. Appl. Phys. (April 2013)

A Kinetics study on modified V-doped FINEMET metallic glass

AIP Conference Proceedings (December 2010)

Laser powder bed fusion of a nanocrystalline Finemet Fe-based alloy for soft magnetic applications Ⓕ

View Online   Export Citation   CrossMark

S. Sadanand,[1] ⓘD M. Rodríguez-Sánchez,[1] ⓘD A. Ghavimi,[2] ⓘD R. Busch,[2] ⓘD P. Sharangi,[3] P. M. Tiberto,[3] ⓘD E. Ferrara,[3] ⓘD G. Barrera,[3] ⓘD L. Thorsson,[4] ⓘD H. J. Wachter,[4] ⓘD I. Gallino,[5] ⓘD and M. T. Pérez-Prado[1,a] ⓘD

AFFILIATIONS

[1]IMDEA Materials Institute, Calle Eric Kandel, 2, 28906 Getafe, Madrid, Spain
[2]Saarland University, Chair of Metallic Materials, Campus C6.3, 66123 Saarbrücken, Germany
[3]INRIM, Istituto Nazionale di Ricerca Metrologica, Strade delle Cacce, 5, 10135 Torino, Italy
[4]Heraeus AMLOY Technologies GmbH, Seligenstädter Straße 100, 63791 Karlstein, Germany
[5]Berlin Institute of Technology, Chair of Metallic Materials, Ernst-Reuter Platz 1, 10587 Berlin, Germany

Note: Paper published as part of the special topic on Laser Manufacturing for Future Mobility.
[a]Author to whom correspondence should be addressed; electronic mail: teresa.perez.prado@imdea.org

ABSTRACT

The aim of this work is to explore the laser powder bed fusion (LPBF) processability window of the nanocrystalline soft magnetic Finemet alloy. With that purpose, several laser power and scan speed values and a meander scanning strategy were probed to process simple geometry specimens. Good dimensional accuracy was obtained within the entire processing window investigated. Relative densities as high as 89% were achieved for processing conditions including high laser power and low scan speeds. The fraction of amorphous phase, which peaked at 49%, was found to be mostly dependent on the scan speed and only slightly influenced by the laser power. The microstructure of the crystalline domains is formed by ultrafine, equiaxed grains with random orientations. Irrespective of the processing conditions, the LPBF-processed samples exhibit a similar saturation magnetization, lower permeability, and higher coercivity than fully amorphous melt-spun ribbons of the same composition. The coercive field of the additively manufactured specimens is fairly independent of the relative density and exhibits a moderate inverse variation with the amorphous fraction. Consistent with earlier works, this study suggests that the average grain size is an important contributor to coercivity.

Key words: nanocrystalline soft magnet, Finemet, laser powder bed fusion, Fe-based alloy.

I. INTRODUCTION

Doubling energy efficiency, including the efficiency of electrical engines, has been recently put forward as a critical mandate to restrict the rise in the average temperature of the Earth by 1.5 K,[1] as it would enable a wider decarbonization of transport. A rough (an optimistic) estimate of the energy losses of the 8×10^9 electric motors in the European Union (EU) (Ref. 2) gives the large amount of ~1350 TWh, which is approximately 30% of the energy

consumed annually in a country like Spain. The development of technologies aimed at reducing losses in electric motors is urgent.

Rotors are components of electric motors whose motion is guided by changing magnetic fields.[3] Ideally, these components should be made of a material with very soft magnetic behavior, i.e., with low coercivity (H_c), high susceptibility (χ), and high saturation magnetization (M_s), as this would reduce the energy required to develop the desired torque.[4] Additionally, rotor materials should have high resistivity to limit the eddy current losses at high

28 February 2025 06:51:44

frequency and high strength to ensure mechanical stability. Traditionally, rotors are composed of laminates of polycrystalline silicon steel,[5,6] a metal that gives rise to relatively high core losses due to the presence of large, elongated grains and of a strong texture. Finding alternative soft magnetic materials and the corresponding manufacturing methods that can shape them into bulk rotor components would, thus, clearly contribute to increasing the overall energy efficiency of electric motors.

Additive manufacturing (AM) methods[7,8] have opened new avenues to produce bulk metallic glass (BMG) components, which were, to date, limited in size because the cooling rates that are achievable in conventional manufacturing are often smaller than those required to freeze the amorphous phase. Laser powder bed fusion (LPBF), for instance, involves cooling rates that may reach up to 10^8 K/s and, thus, LPBF of BMGs is a rapidly expanding field.[9–13] Most works to date have focused on Zr-based alloys due to their higher glass forming ability (GFA) and to their larger ductility, which makes them more resilient to the thermal residual stresses that are accumulated during processing. Conversely, Fe-based BMGs,[14] which have an excellent soft magnetic behavior, have been less investigated due to their lower GFA and their inherent brittleness, which may even lead to pulverization upon the application of external loads.

Although the study of LPBF of Fe-based BMG alloys is still in its infancy, research has been underway during the past few years to tackle the complex existing challenges.[15–27] The alloys investigated include $Fe_{54.35}Cr_{18.47}Mn_{2.05}Mo_{13.93}W_{5.77}B_{3.22}C_{0.90}Si_{1.32}$ (wt. %),[15] $Fe_{74}Mo_4P_{10}C_{7.5}B_{2.5}Si_2$ (wt. %),[16] $Fe_{43.7}Co_{7.3}Cr_{14.7}Mo_{12.6}C_{15.5}B_{4.3}Y_{1.9}$ (at. %),[17,18] FeCrMoBC,[19–22] $Fe_{68.3}C_{6.9}Si_{2.5}B_{6.7}P_{8.7}Cr_{2.3}Mo_{2.5}Al_{2.1}$ (at. %),[23] ${(Fe^{0.6}Co^{0.4})_{0.75}B_{0.2}Si_{0.05}}_{96}Nb_4$ (at. %),[24] and $Fe_{73.7}Si_{11}B_{11}C_2Cr_{2.28}$ (at. %) (Kuamet 6B2).[25–28] Most of these studies are aimed at relating the LPBF processing parameters [mainly laser power (P) and scan speed (v)] to the resulting structures and to the mechanical and/or magnetic properties of the manufactured amorphous/crystalline composites. It is currently widely recognized that the processing conditions that lead to a high density (high laser power and/or low scan speed) in general result in low fractions of the amorphous phase, and vice versa.[11] Thus, achieving simultaneously high values of density and large volume fractions of the glassy phase remains an outstanding challenge in AM of Fe-based BMGs.

Fe-based nanocrystalline alloys such as Finemet (Fe-Si-B-Nb-Cu)[29] have also been widely explored over the past few decades as promising soft magnetic materials[30] due to their excellent combination of properties, including a large M_s, a high resistivity (double that of the widely used Fe-3 wt. % Si), and an extremely small H_c[31] (up to an order of magnitude lower than that of silicon steel). Overall, it is recognized that the use of Finemet in electric motors could potentially lead to a drastic reduction of core losses.[32] The most common method that has so far been utilized to manufacture nanocrystalline Finemet components is heat treatment of melt-spun glasses,[33,34] as the low GFA of this alloy severely hinders the fabrication of bulk components by casting methods. Alternative techniques include mechanical alloying and milling[35] as well as cold sintering and spark plasma sintering,[36,37] which, however, allow a smaller control of crystallization. To date, a limited number of studies have attempted to process Finemet samples using laser-based methods.[38,39] In particular, Conteri et al.[38] and Borkar

et al.[39] report the use of laser engineering net shaping (LENS) to produce FeSiBNbCu alloys from a mixture of elemental iron, silicon, boron, niobium, and copper powders. However, since the cooling rates involved in the LENS process (10^4–10^5 K/s) are several orders of magnitude smaller than those required to stabilize the amorphous phase in Finemet (10^6–10^8 K/s), the specimens manufactured under all the investigated conditions consist of a high fraction of relatively large dendritic grains and are, thus, endowed with a semihard magnetic behavior. Other studies have attempted nanocrystallization via laser annealing of amorphous ribbons.[40,41] Finally, a single study was found on LPBF of Finemet,[42] where a continuous laser is utilized to manufacture cylindrical specimens within a processing region comprising laser power values between 60 and 350 W and scan speeds between 250 and 3000 mm/s was explored. The use of LPBF to additively manufacture Finemet alloy parts remains underexplored.

The aim of this work is to explore the feasibility of additively manufacturing the Finemet alloy using pulsed wave LPBF. A processing campaign including variations in the laser powder and the scan speed is carried out in order to establish a relationship between the processing parameters, the (micro)structure, and the magnetic behavior. This work constitutes a pioneer study on the fundamentals of LPBF processing of Finemet alloys aimed ultimately at the production of complex-shaped soft magnetic components with reduced core losses.

II. EXPERIMENTAL PROCEDURE

The material used in this work is a Finemet (Fe-Si-B-Nb-Cu) powder alloy whose composition is summarized in Table I. Powder production was conducted by spinning water gas atomization at

TABLE I. Chemical composition of the Finemet alloy.

Element	Weight (%)
Iron	Balance
Silicon	7.40–8.00
Niobium	5.46–5.86
Boron	1.78–2.18
Copper	1.19–1.39
Chromium	≤0.10
Carbon	≤0.07

TABLE II. LPBF processing conditions.

Sample	Laser power (W)	Scan speed (mm/s)	VED (J/mm³)
1	40	350	47.6
2	40	500	33.3
3	40	650	25.6
4	40	800	20.8
5	60	500	50.0
6	60	650	38.5
7	60	800	31.2
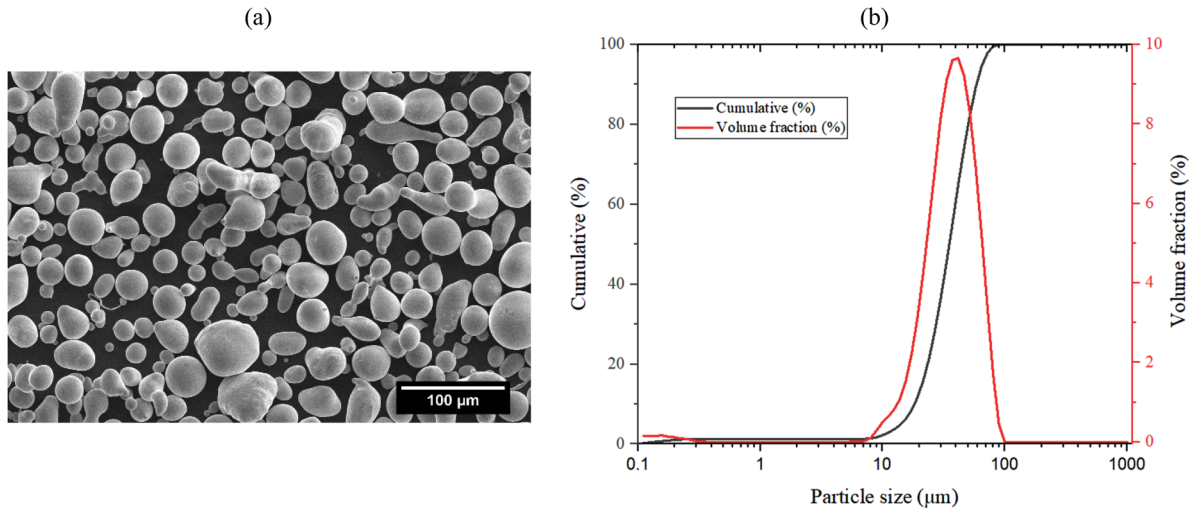
FIG. 1. (a) SEM secondary electron micrograph showing the particle morphology; (b) particle size distribution.
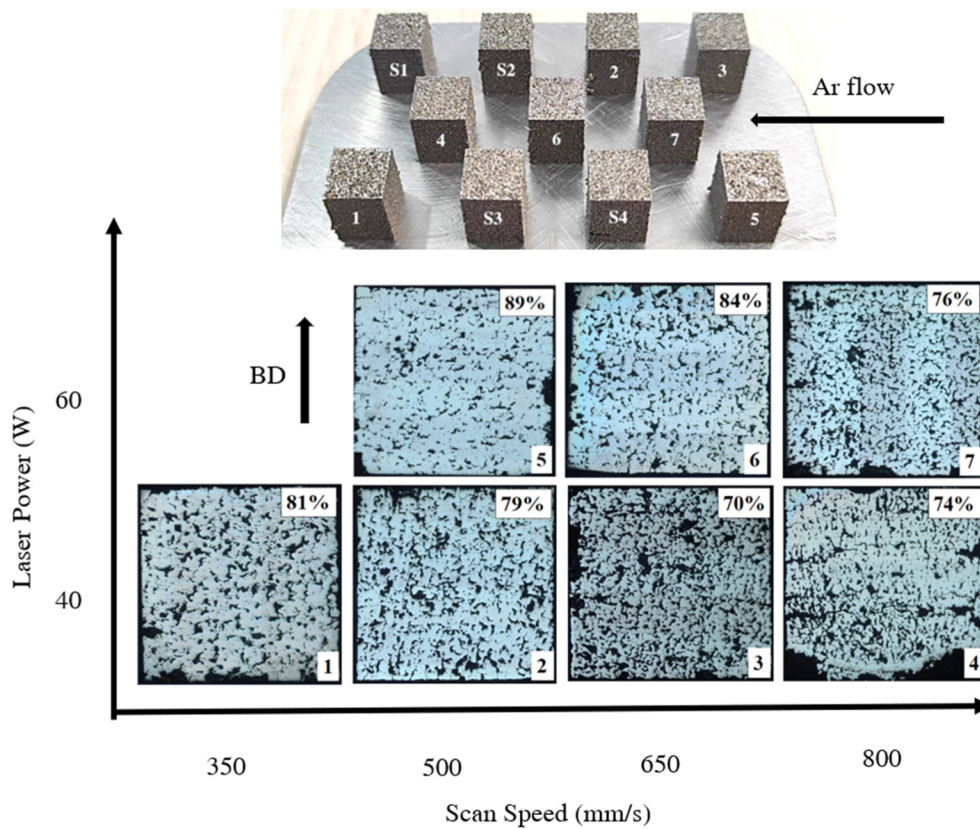
FIG. 2. Optical micrographs depicting the defect structure of the (8 × 8 × 9.5) mm³ prisms manufactured by LPBF with the different parameter combinations that are listed in Table II. The density corresponding to each sample, measured by image analysis from the optical micrographs, is indicated in the top right corner of the corresponding image. The inset illustrates the printed samples on the build plate.

28 February 2025 06:51:44

TABLE III. Defect structure (density, area fraction of pores and cracks) and volume fraction of amorphous phase corresponding to samples manufactured using different LPBF parameter combinations.

Sample	Density (%)	Area fraction of pores (%)	Area fraction of cracks (%)	Volume fraction of amorphous phase (%)	H_c (A/m)
1	81	19.1	0.7	13	1450
2	79	21.4	1.1	36	1260
3	70	29.7	1.6	46	1250
4	74	25.5	2.3	45	1360
5	89	10.7	1.0	27	1260
6	84	16.0	0.9	38	1210
7	76	24.3	1.4	49	1180

Epson Atmix. A range of complementary characterization techniques were utilized for powder characterization. The particle morphology was examined by scanning electron microscopy (SEM) using an APREO 2S microscope (Thermo Fischer Scientific) operating at a voltage of 5 kV, a current of 43 μA, and a working distance of 10 mm. The particle size distribution (PSD) was determined using a Bettersizer ST laser analyzer with the aid of the Bettersize V.8.0 system software. A qualitative analysis of the phase distribution of the powders was carried out first via x-ray diffraction (XRD) in an Empyrean PANanalytical x-ray diffractometer using Cu-$k\alpha$ radiation ($\lambda = 1.5405$ Å) within a 2θ range from 30° to 120°. The 2θ increment was 0.05° and the acquisition time amounted to 300 s. The amorphous fraction (AM%) was also quantified by differential scanning calorimetry (DSC) using a power-compensated Perkin-Elmer 8000 Hyper DSC device. The actual value was estimated from the ratio of the crystallization enthalpy of the sample to that of a melt-spun ribbon of the same composition ($AM\% = \Delta H_{cr,\text{sample}}/\Delta H_{cr,\text{ribbon}}$) that was used as a reference. The flowability as well as the apparent (D_a) and tapped (D_t) densities were measured using a Hall flowmeter following standardized methods. D_t was estimated by recording the change in volume of the powders with a periodic tapping for 60 s. The compressibility index and the Hausner ratio were calculated from the density values as indicated by Eqs. (1) and (2), respectively,

$$\text{Compressibility index} = 100 \star \frac{Dt - Da}{Da}, \quad (1)$$
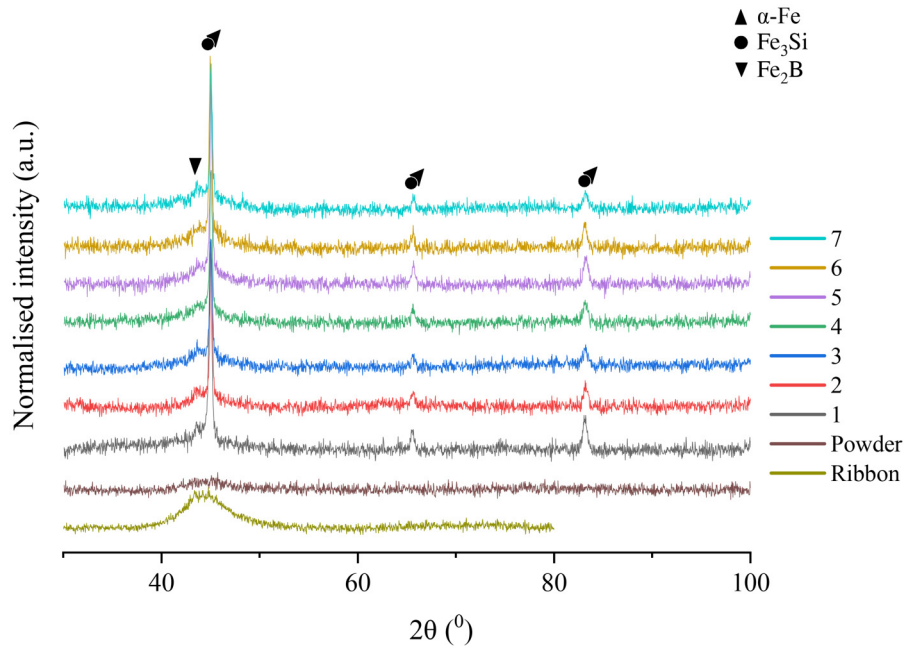

FIG. 3. Comparison of the x-ray patterns corresponding to the seven samples manufactured by LPBF using different combinations of processing parameters (Table II) with that of the fully amorphous powders.
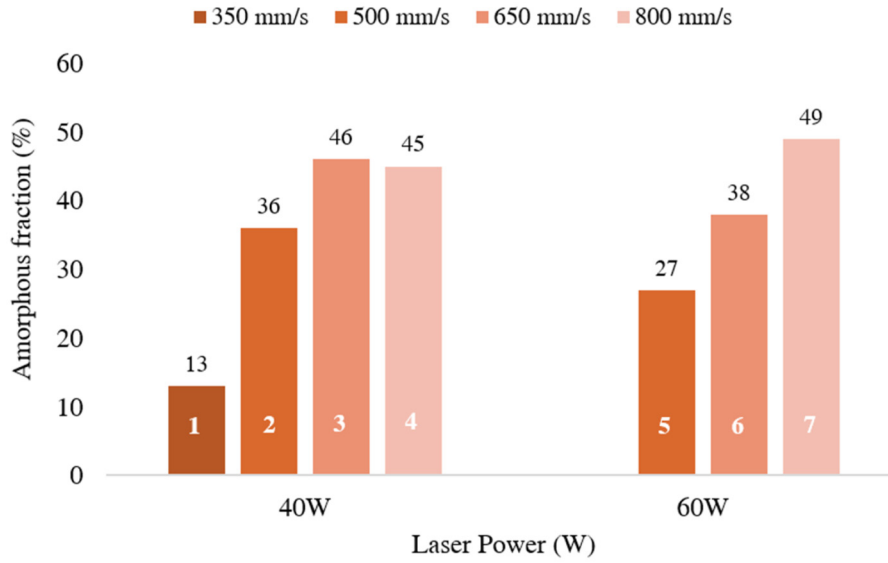
FIG. 4. Volume fraction of the amorphous phase in the LPBF-manufactured parts as a function of laser power and the scan speed.

$$\text{Hausner ratio} = \frac{Dt}{Da}. \qquad (2)$$

LPBF of $(8 \times 8 \times 9.5)$ mm^3 prisms was performed using a pulsed-laser Renishaw AM400 machine furnished with a reduced build volume (RBV) platform containing a 316L steel substrate. A simple meander scan strategy with a rotation of 67° after each layer was utilized in all cases in order to better understand the processing-(micro)structure-property relationships. The hatch distance (h), the point distance (pd), the spot size (ss), and the layer thickness (t) were kept constant in all fabrications. A fixed inter-pulse delay of 10 μs was utilized. In particular, the values of these parameters were $h = 80\,\mu$m, pd $= 80\,\mu$m, ss $= 63\,\mu$m, and $t = 30\,\mu$m. Table II summarizes the seven LPBF parameter sets investigated, which include variations of P from 40 to 60 W and of v from 350 to 800 mm/s. The latter was altered by changing the exposure time (t_{exp}). Higher power values led to a loss of dimensional stability and, thus, have not been utilized in the present study. Finally, the equivalent volumetric energy density (VED) values were also calculated and are listed in Table II next to the corresponding processing parameter set.

The defect structure of the LPBF-manufactured prisms was first examined by optical microscopy (OM) using an Olympus BX51 microscope and a wide area of the sample was imaged by stitching together micrographs captured at a magnification of 5×. The software IMAGEJ was then utilized to classify and to separate different defect types (pores and cracks) from the bulk. In particular, Fiji's machine learning-assisted segmentation plug-in, the WEKA trainable segmentation package,[43] was used for this purpose. Samples for OM examination were first cut using a Secotom disc cutting machine, and they were then ground sequentially with 320,

600, 1200, and 2000 grit SiC papers. Finally, surface finishing was conducted by mechanical polishing with diamond suspensions of average particle sizes amounting, consecutively, to 6, 3, and 1 μm. The phase distribution and the fraction of the amorphous phase in the LPBF-manufactured specimens were characterized, respectively, by XRD and by DSC following a similar procedure to that utilized for the powders, which is explained above. The sample preparation procedure for XRD characterization consisted of the same cutting, grinding, and mechanical polishing steps described above for the preparation of sample surfaces for OM examination. Sample preparation for DSC measurements included cutting with a slow speed diamond saw specimens of approximately 20 mg in weight. The
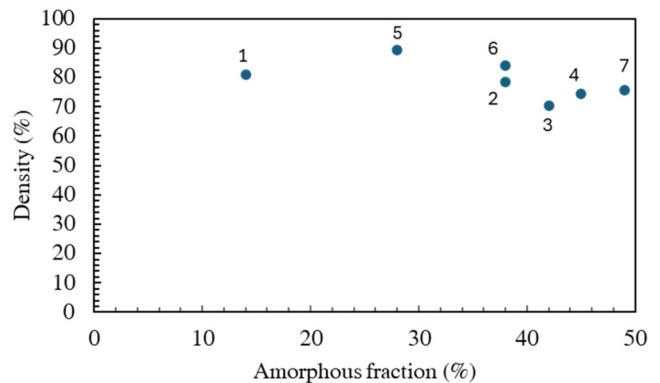
FIG. 5. Variation of the relative density with respect to the amorphous fraction in all the LPBF-manufactured Finemet samples.
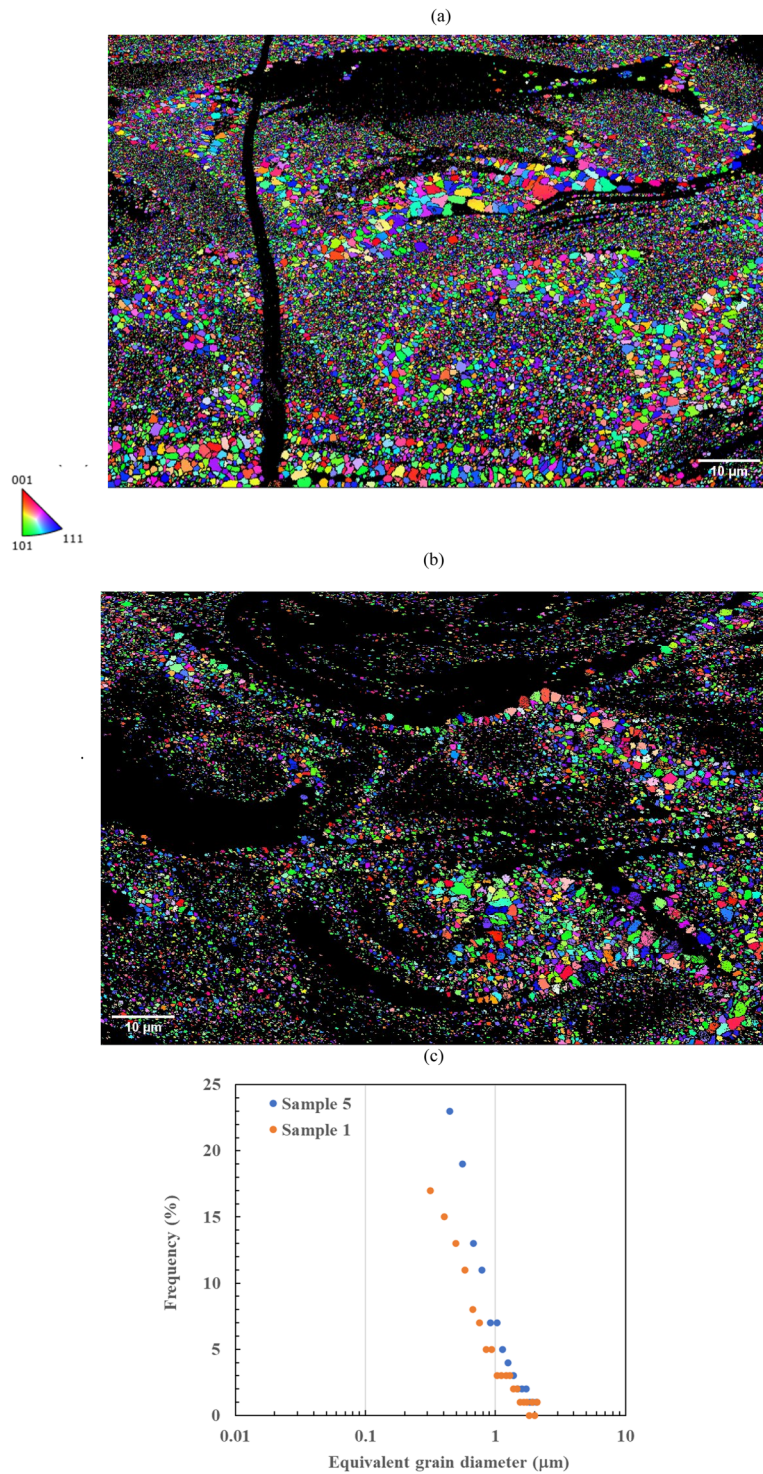
FIG. 6. EBSD inverse pole figure maps in the BD corresponding to representative crystalline regions of (a) sample 5 (60 W, 500 mm/s, density = 89%, fraction of amorphous phase = 27%) and (b) sample 1 (40 W, 350 mm/s, density = 81%, fraction of amorphous phase = 13%). (c) Distribution of equivalent grain diameters in samples 5 (blue dots) and 1 (orange dots).

28 February 2025 06:51:44

microstructure (grain size, shape, and texture) of the crystalline regions was examined by electron backscattered diffraction (EBSD) using an Apreo 2S (ThermoFisher Scientific) field emission gun scanning electron microscope (FEGSEM) equipped with an Oxford Instruments detector, a CCD camera, and the Aztec data acquisition and analysis software package. The measuring conditions included an accelerating voltage of 20 kV and a step size of 70 nm.

Room-temperature magnetization behavior of the LPBF-manufactured specimens was studied by means of a vibrating sample magnetometer (VSM, Lakeshore) using a continuous measurement procedure in the applied field range ±1300 kA/m. Hysteresis loops were measured at room temperature and, from them, M_s and H_c were estimated for each sample after appropriate subtraction of the diamagnetic signal from the sample holder.

III. RESULTS AND DISCUSSION

Figure 1(a) is an SEM secondary electron micrograph illustrating the morphology of the Finemet feedstock powder. The particles have ellipsoidal to spherical shape, with a small fraction of satellites. The size distribution, plotted in Fig. 1(b), is monomodal and it is characterized by D_{10}, D_{50}, and D_{90} values of 18, 35, and 58 μm, respectively. The Hall flowability of the powder is 18 s, and D_a and D_t amount, respectively, to 3.9 and 4.3 g/cm^3. The compressibility index and the Hausner ratio, calculated using Eqs. (1) and (2), are 1.08 and 7.87, respectively. These values are considered indicators of an "excellent" flow character.[44]

Figure 2 shows, on the one hand, the LPBF-manufactured prisms that were processed using the parameter combinations 1–7 that are listed in Table II. It can be seen that a good dimensional accuracy is achieved for all the printing conditions. Optical micrographs of a cross section parallel to BD that depicts the defect structure of all the Finemet printed prisms are also displayed in Fig. 2. The density corresponding to each sample, measured by image analysis from the optical micrographs, is indicated in the top right corner of the corresponding image. It can be seen that the part density increases with increasing P and with decreasing v, as generally observed in metallic glasses that are manufactured in the conduction mode,[11] as well as for other alloys. Table III lists the density values corresponding to the seven LPBF-manufactured samples, which range from 70% to 89%. This table also shows the area fraction of cracks, which remains in general below ~2%, and the fraction of lack of fusion pores, which varies between ~11% and ~30%. In order to test the robustness of the LPBF process, six additional prisms (R1–R6) were manufactured with the conditions of sample 5 (60 W, 500 mm/s) (Supplementary Table 1).[47] The defect structure of these samples is shown by means of the corresponding optical micrographs along a plane parallel to BD in Supplementary Fig. 1,[47] and the corresponding values of the density and the fraction of pores and of cracks are included in Supplementary Table 2.[47] The average value of the density of sample 5 plus the R1–R6 samples amounts to 88.0% ± 0.9%. The small error obtained attests to the robustness of the study. An additional set of prisms with the conditions corresponding to samples 1–4, termed S1–S4, were also manufactured and the corresponding data are also included in Supplementary Tables 1 and 2,[47] as well
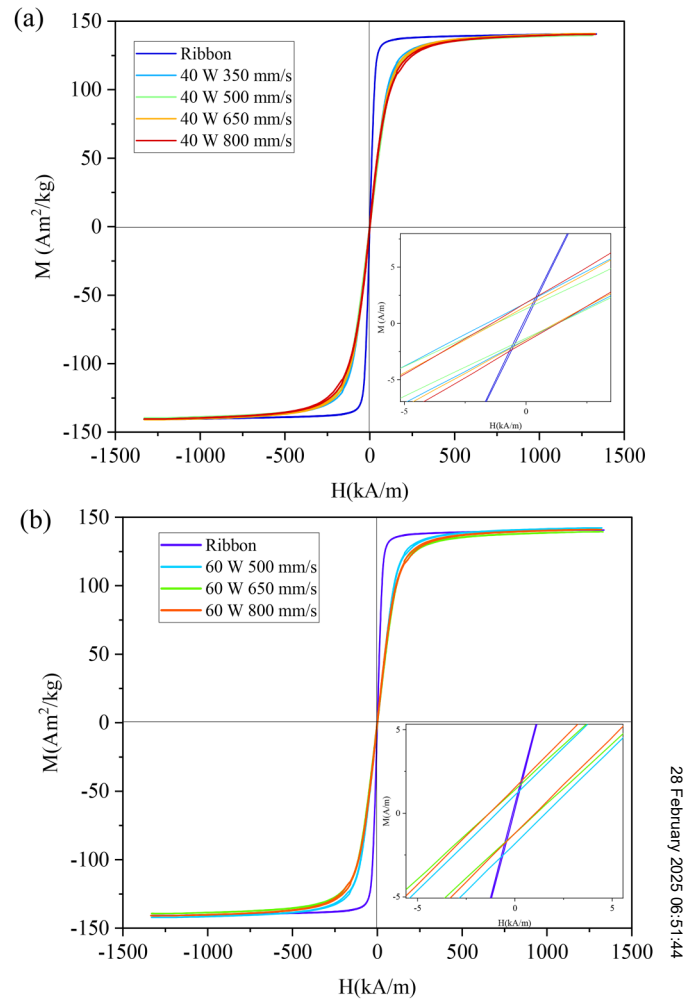
FIG. 7. Room-temperature hysteresis loops corresponding to all LPBF-manufactured samples. Each plot shows the curves corresponding to samples manufactured using a common laser power value: (a) 40 and (b) 60 W.

as in Supplementary Fig. 1.[47] Again, the similarity in the values obtained attest to the reproducibility of the study.

Figure 3 compares the XRD diagrams corresponding to all the Finemet LPBF-manufactured parts with that of the atomized powders and of a melt-spun ribbon of the same composition. The powders and the ribbon are fully amorphous, as indicated by the sole presence of a wide hump at 45° in their XRD patterns. Irrespective of the processing conditions, the patterns of the LPBF-manufactured prisms consist of a superposition of a wide hump located around 45° and sharp peaks corresponding to the phases α-Fe/Fe$_3$Si, which cannot be distinguished by XRD, and to the intermetallic Fe$_2$B$_6$. That is, XRD measurements confirm, qualitatively, the presence of an amorphous/crystalline composite in all the printed parts. Figure 4 depicts the variation of the volume fraction of the amorphous phase, measured by DSC, with the laser

28 February 2025 06:51:44
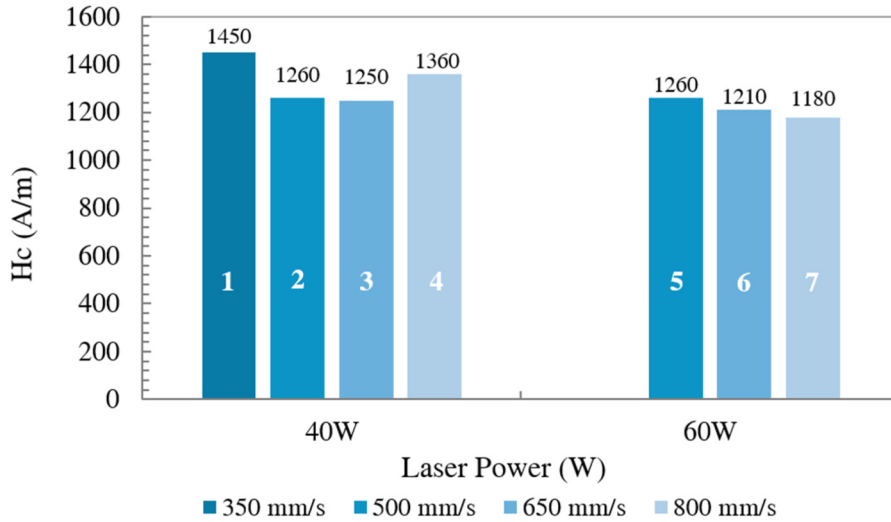
FIG. 8. Coercivity of the LPBF-processed Finemet samples as a function of the laser power and the scan speed.
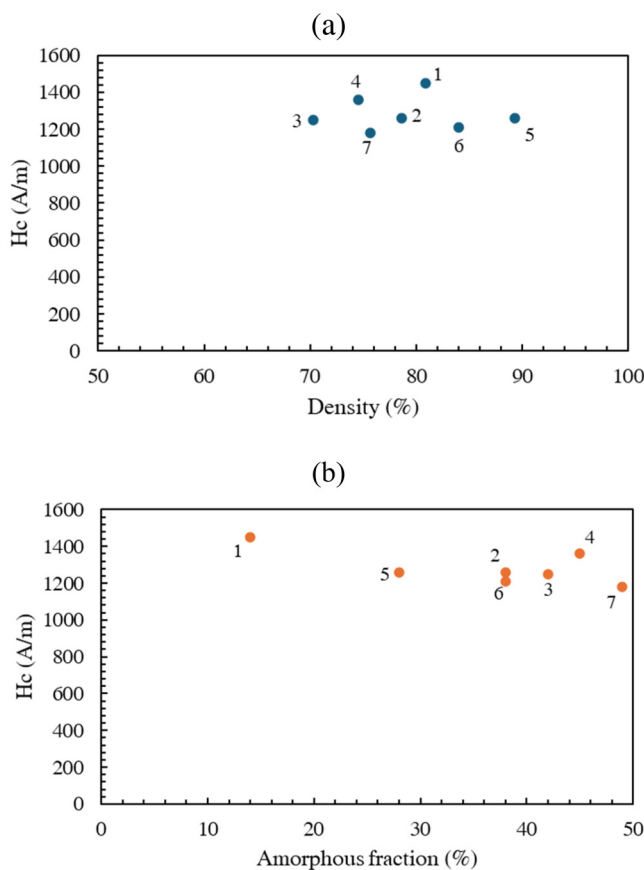
FIG. 9. Variation of the coercive field with (a) the relative sample density and (b) the volume fraction of amorphous phase in the seven Finemet LPBF-manufactured samples.

power and with the scan speed. Within the range of processing parameters investigated, the fraction of the glassy phase varies from 13% to 49%. Figure 4 evidences a strong influence of the scan speed on the fraction of amorphous material, which increases significantly with increasing v. Comparison of Figs. 2 and 4 reveals that the processing parameter windows that give rise to the highest densities and to the highest amorphous fractions, respectively, do not overlap. Figure 5 shows the variation of the relative density with respect to the amorphous fraction for all the LPBF-manufactured samples. Even though the data presented is limited, it can be seen that the highest AM% is, indeed, obtained in the samples with the lowest density.

The microstructure of the crystalline regions was found to be fairly independent of the processing conditions. Figure 6 illustrates two EBSD inverse pole figure maps in the BD captured in representative crystalline regions of samples 5 (60 W, 500 mm/s, density = 89%, AM% = 27%) [Fig. 6(a)] and 1 (40 W, 350 mm/s, density = 81%, AM% = 13%) [Fig. 6(b)]. It can be seen that, in both cases, the microstructure is formed by fine and equiaxed crystallites that are randomly oriented. Figure 6(c) shows, additionally, that the distribution of grain sizes, measured as the equivalent grain diameter by EBSD, is also similar in both cases. For both samples, crystallite sizes lie mostly between ~250 nm and 2 μm, with average values ($\langle d \rangle$) of 814 ± 386 nm for sample 5 and 710 ± 395 nm for sample 1. It must be taken into account that under the current observation conditions EBSD might not be able to detect the smallest grains and, therefore, the presence of grains with diameters smaller than 250 nm cannot be completely ruled out. Nevertheless, as can be seen in Figs. 6(a) and 6(b), the fraction of indexed grains is relatively high.

Room-temperature hysteresis loops of all Finemet LPBF-manufactured samples are reported in Fig. 7. In particular, the curves of specimens processed with laser power values of 40 [Fig. 7(a)] and 60 W [Fig. 7(b)] are shown in separate graphs. In the inset, a low-field magnification is shown to evidence the coercivity values. The area of the plot close to the origin is depicted at
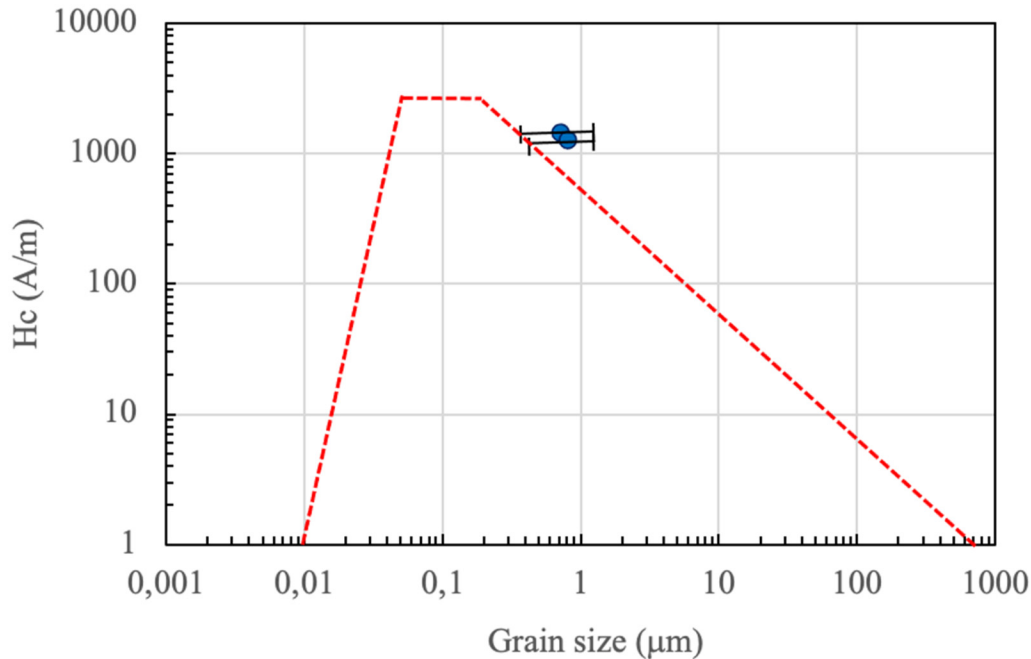
FIG. 10. Dependence of coercivity on the average grain size ($\langle d \rangle$) of soft magnetic materials in the whole ranges of structural correlation lengths [red dotted line, data extracted from (Ref. 32)]. The blue dots indicate (D, H_c) data measured in samples 1 and 5 of the current study.

higher magnification as an inset. The magnetization behavior of a fully amorphous melt-spun ribbon is also included in the plots for comparison. In general, in comparison to the ribbon, the LPBF-manufactured samples exhibit similar saturation magnetization values, reached at higher fields with respect to the amorphous ribbons, lower permeability, and higher coercivity. The coercive field value of the ribbon (13 A/m), being below the sensitivity of the VSM, was measured by using a digital wattmeter at 5 Hz exploiting a conventional fluxmetric technique. Figure 8 illustrates the variation of the coercive field as a function of the LPBF processing parameters and, in particular, of the laser power (P) and of the scan speed (v). For a constant v, different P values do not affect H_c substantially, although a minor decrease in H_c is observed with increasing P. Conversely, by increasing v between 350 and 800 mm/s, minor changes in H_c can be observed. In particular, for $P = 40$ W, the lowest H_c values are obtained at intermediate scan speeds of 500 and 650 mm/s. For $P = 60$ W, H_c decreases slightly when increasing v from 500 to 800 mm/s. The H_c values corresponding to the processing conditions investigated in this work are summarized in Table III. H_c values range in the interval from 1180 to 1450 A/m. The average value of H_c in sample 5 plus the R1–R6 samples (see Supplementary Table 2)[47] amounts to 1328 ± 26 A/m. The small error obtained attests to the robustness of the study. The H_c values corresponding to the S1–S4 prisms manufactured with the conditions corresponding to samples 1–4 are also included in Supplementary Table 2.[47] Again, the similarity in the values obtained attests to the reproducibility of the study.

Figure 9 illustrates the relationship between H_c and two key microstructure features such as the sample density and the amorphous fraction. H_c turns out to be substantially independent of the density. Concerning the amorphous fraction, a slight dependence is observed. In particular, an increase in the fraction of the amorphous phase from 13% to 49% (i.e., 3.8 times) leads to a decrease in H_c of about 18%. This behavior turned out to be different from what is observed in amorphous Fe-based metallic glasses such as Kuamet 6B2,[45] where the coercive field halves when the amorphous fraction increases by a comparative amount.

The existence of a strong dependence of H_c on the average grain size ($\langle d \rangle$) in nanocrystalline soft magnetic materials is well known in the literature.[32,46] Figure 10 plots the dependence of the coercive field on $\langle d \rangle$ of soft magnetic materials in the whole ranges of structural correlation lengths (red dotted line).[32] In the ultrafine grain regime ($\langle d \rangle \lesssim 80$ nm), H_c is proportional to $\langle d \rangle$.[6] However, when $\langle d \rangle \gtrsim 0.1$–$1\,\mu$m,[32] H_c decreases rapidly with increasing grain size. The blue dots in Fig. 10 indicate the ($\langle d \rangle$, H_c) data corresponding to the LPBF-manufactured sample 5, with the highest H_c (1450 A/m), and sample 1, with a lower H_c (1260 A/m). Both data points fit well with the overall trend depicted by the dashed red line, suggesting that the grain size is a key contributor to the coercivity. The small variations of H_c found in the seven LPBF-manufactured samples would be consistent with the presence of similar $\langle d \rangle$ values. This study suggests that reducing the coercivity to levels that are comparable to those of melt-spun ribbons (13 A/m) would require the stabilization of crystalline microstructures with

28 February 2025 06:51:44

average grain sizes either close to 10 nm or of the order of several hundred microns.

IV. CONCLUSIONS

The aim of this work was, first, to investigate the feasibility of manufacturing the Finemet nanocrystalline soft-magnetic alloy via pulsed wave laser powder bed fusion. With that goal, simple geometry specimens were produced using a range of laser power and scan speed combinations and the processing parameters were subsequently related to the (micro)structure and to the magnetic behavior. The following conclusions can be drawn from the present study:

1. Finemet prisms with dimensions $8 \times 8 \times 9.5$ mm^3 were manufactured with good dimensional accuracy within a processing window including laser power values ranging from 40 to 60 W and scan speeds comprised in a 350–800 mm/s interval. The relative density increased with increasing P and decreasing v, while the amorphous fraction was directly proportional to v but almost independent of P. Densities as high as 89% and amorphous fractions as large as 49% were obtained within the investigated processing window. The microstructure of the crystalline regions was found to be formed by ultrafine, equiaxed grains with random orientations.
2. In comparison to fully amorphous melt-spun Finemet ribbons, the LPBF-processed samples exhibit a similar saturation magnetization, lower permeability, and higher coercivity, irrespective of the processing conditions.
3. The coercive field of the additively manufactured specimens is fairly independent of the relative density and exhibits a moderate inverse variation with the amorphous fraction. The average grain size appears to be a key contributor to H_c.

.

AUTHOR DECLARATIONS

Conflict of Interest

The authors have no conflicts to disclose.

Author Contributions

S. Sadanand: Investigation (lead); Methodology (equal); Writing – original draft (equal); Writing – review & editing (equal). **M. Rodríguez-Sánchez:** Investigation (equal); Methodology (equal); Writing – original draft (equal); Writing – review & editing (equal). **A. Ghavimi:** Investigation (equal); Methodology (equal); Writing – review & editing (equal). **R. Busch:** Funding acquisition (equal); Resources (equal); Supervision (equal); Writing – review & editing (equal). **P. Sharangi:** Investigation (equal); Methodology (equal); Writing – original draft (equal); Writing – review & editing (equal). **P. M. Tiberto:** Funding acquisition (equal); Resources (equal); Supervision (equal); Writing – original draft (equal); Writing – review & editing (equal). **E. Ferrara:** Investigation (equal); Supervision (equal); Writing – original draft (equal); Writing – review & editing (equal). **G. Barrera:** Investigation (equal); Methodology (equal); Writing – original draft (equal); Writing – review & editing (equal). **L. Thorsson:** Funding acquisition (equal); Methodology (equal); Writing – review & editing (equal). **H. J. Wachter:** Funding acquisition (equal); Methodology (equal); Writing – review & editing (equal). **I. Gallino:** Funding acquisition (lead); Resources (equal); Supervision (equal); Writing – review & editing (equal). **M. T. Pérez-Prado:** Funding acquisition (equal); Resources (equal); Supervision (equal); Writing – original draft (equal); Writing – review & editing (equal).

DATA AVAILABILITY

The data that support the findings of this study are available from the corresponding author upon reasonable request.

REFERENCES

[1]"Tripling renewable power and doubling energy efficiency by 2030: Crucial steps towards 1.5°C," International Renewable Energy Agency (IRENA) Report (2023).

[2]See https://commission.europa.eu/energy-climate-change-environment/standards-tools-and-labels/products-labelling-rules-and-requirements/energy-label-and-ecodesign/energy-efficient-products/electric-motors-and-variable-speed-drives_en#energy-savings for information on the estimation of the number of electric motors in the EU as well as their energy consumption.

[3]A. Hughes and B. Drury, *Electric Motors and Drives* (Newnes, Amsterdam, 2013).

[4]O. Gutfleisch, M. A. Willard, E. Brück, C. H. Chen, S. G. Sankar, and J. P. Liu, "Magnetic materials for the 21st century: Stronger, lighter, and more energy efficient," Adv. Mater. **23**, 821–842 (2011).

[5]A. Krings, A. Boglietti, A. Cavagnino, and S. Sprague, "Soft magnetic material status and trends in electric machines," IEEE Trans. Ind. Electron. **64**, 2405–2414 (2017).

[6]G. Ouyang, X. Chen, Y. Liang, C. Macziewski, and J. Cui, "Review of Fe-6.5 wt. %Si high silicon steel—A promising soft magnetic material for sub-kHz application," J. Magn. Magn. Mater. **481**, 234–250 (2019).

[7]T. DebRoy, H. L. Wei, J. S. Zuback, T. Mukherjee, J. W. Elmer, J. O. Milewski, A. M. Beese, A. Wilson-Heid, A. De, and W. Zhang, "Additive manufacturing of metallic components—Process, structure and properties," Prog. Mater. Sci. **92**, 112–224 (2018).

[8]D. Herzog, V. Seyda, E. Wycisk, and C. Emmelmann, "Additive manufacturing of metals," Acta Mater. **117**, 371–392 (2016).

[9]H. R. Lashgari, M. Ferri, and S. Li, "Additive manufacturing of bulk metallic glasses: Fundamental principle, current/future developments and applications," J. Mater. Sci. Technol. **119**, 131–149 (2022).

[10]N. Sohrabi, J. Jhabvala, and R. E. Logé, "Additive manufacturing of bulk metallic glasses process, challenges and properties: A review," Metals **11**, 1279 (2021).

[11]Ł. Żrodowski, R. Wróblewski, M. Leonowicz, B. Morończyk, T. Choma, J. Ciftci, W. Święszkowski, A. Dobkowska, E. Ura-Bińczyk, P. Błyskun,

J. Jaroszewicz, A. Krawczyńska, K. Kulikowski, B. Wysocki, T. Cetner, G. Moneta, X. Li, L. Yuan, A. Małachowska, R. Chulist, and C. Żrodowski, "How to control the crystallization of metallic glasses during laser powder bed fusion? Towards part-specific 3D printing of *in situ* composites," Addit. Manuf. **76**, 103775 (2023).

[12]H. Liu, Q. Jiang, J. Huo, Y. Zhang, W. Yang, and X. Li, "Crystallization in additive manufacturing of metallic glasses: A review," Addit. Manuf. **36**, 101568 (2020).

[13]S. Hadibeik, H. Ghasemi-Tabasi, A. Burn, S. Lani, F. Spieckermann, and J. Eckert, "Controlling the glassy state toward structural and mechanical enhancement: Additive manufacturing of bulk metallic glass using advanced laser beam shaping technology," Adv. Funct. Mater. **34**, 2311118 (2024).

[14]H. X. Li, Z. C. Lu, S. L. Wang, Y. Wu, and Z. P. Lu, "Fe-based bulk metallic glasses: Glass formation, fabrication, properties and applications," Prog. Mater. Sci. **103**, 235–318 (2019).

[15]X. D. Nong, X. L. Zhou, and Y. X. Ren, "Fabrication and characterization of Fe-based metallic glasses by selective laser melting," Opt. Laser Technol. **109**, 20–26 (2019).

[16]S. Pauly, L. Löber, R. Petters, M. Stoica, S. Scudino, U. Kühn, and J. Eckert, "Processing metallic glasses by selective laser melting," Mater. Today **16**, 37–41 (2013).

[17]D. Ouyang, W. Xing, N. Li, Y. Li, and L. Liu, "Structural evolutions in 3D-printed Fe-based metallic glass fabricated by selective laser melting," Addit. Manuf. **23**, 246–252 (2018).

[18]N. Li, J. Zhang, W. Xing, D. Ouyang, and L. Liu, "3D printing of Fe-based bulk metallic glass composites with combined high strength and fracture toughness," Mater. Des. **143**, 285–296 (2018).

[19]P. Bordeenithikasem, D. C. Hofmann, S. Firdosy, N. Ury, E. Vogli, and D. R. East, "Controlling microstructure of FeCrMoBC amorphous metal matrix composites via laser directed energy deposition," J. Alloys Compd. **857**, 157537 (2021).

[20]Y. Zou, Z. Qiu, C. Tan, Y. Wu, K. Li, and D. Zeng, "Microstructure and mechanical properties of Fe-based bulk metallic glass composites fabricated by selective laser melting," J. Non-Cryst. Solids **538**, 120046 (2020).

[21]Y. Zou, Y. Wu, K. Li, C. Tan, Z. Qiu, and D. Zeng, "Selective laser melting of crack-free Fe-based bulk metallic glass via chessboard scanning strategy," Mater. Lett. **272**, 127824 (2020).

[22]L. Wang, H. Wang, Y. Liu, Z. Fu, T. Peng, J. Shen, S. Zhou, M. Yan, G. Wang, and Y. Dai, "Selective laser melting helps fabricate record-large bulk metallic glass: Experiments, simulation and demonstrative part," J. Alloys Compd. **808**, 151731 (2019).

[23]H. Y. Jung, S. J. Choi, K. G. Prashanth, M. Stoica, S. Scudino, S. Yi, U. Kühn, D. H. Kim, K. B. Kim, and J. Eckert, "Fabrication of Fe-based bulk metallic glass by selective laser melting: A parameter study," Mater. Des. **86**, 703–708 (2015).

[24]N. Luo, C. Scheitler, N. Ciftci, F. Galgon, Z. Fu, V. Uhlenwinkel, M. Schmidt, and C. Körner, "Preparation of Fe-Co-B-Si-Nb bulk metallic glasses by laser powder bed fusion: Microstructure and properties," Mater. Charact. **162**, 110206 (2020).

[25]Y. G. Nam, B. Koo, M. S. Chang, S. Yang, J. Yu, Y. H. Park, and J. W. Jeong, "Selective laser melting vitrification of amorphous soft magnetic alloys with help of double-scanning-induced compositional homogeneity," Mater. Lett. **261**, 127068 (2020).

[26]L. Thorsson, M. Unosson, M. T. Pérez-Prado, X. Jin, P. Tiberto, G. Barrera, B. Adam, N. Neuber, A. Ghavimi, M. Frey, R. Busch, and I. Gallino, "Selective laser melting of a Fe-Si-Cr-B-C-based complex-shaped amorphous soft-magnetic electric motor rotor with record dimensions," Mater. Des. **215**, 110483 (2022).

[27]Ł. Żrodowski, B. Wysocki, R. Wróblewski, A. Krawczyńska, B. Adamczyk-Cieślak, J. Zdunek, P. Błyskun, J. Ferenc, M. Leonowicz, and W. Święszkowski, "New approach to amorphization of alloys with low glass forming ability via selective laser melting," J. Alloys Compd. **771**, 769–776 (2019).

[28]M. G. Özden and N. A. Morley, "Optimizing laser additive manufacturing process for Fe-based nano-crystalline magnetic materials," J. Alloys Compd. **960**, 170644 (2023).

[29]Y. Yoshizawa, S. Oguma, and K. Yamauchi, "New Fe-based soft magnetic alloys composed of ultrafine grain structure," J. Appl. Phys. **64**, 6044–6046 (1988).

[30]M. E. McHenry, M. A. Willard, and D. E. Laughlin, "Amorphous and nanocrystalline materials for applications as soft magnets," Prog. Mater. Sci. **44**, 291–433 (1999).

[31]G. Herzer, "Grain structure and magnetism of nanocrystalline ferromagnets," IEEE Trans. Magn. **25**, 3327–3329 (1989).

[32]T. Gheiratmand and H. R. Madaah Hosseini, "Finemet nanocrystalline soft magnetic alloy: Investigation of glass forming ability, crystallization mechanism, production techniques, magnetic softness and the effect of replacing the main constituents by other elements," J. Magn. Magn. Mater. **408**, 177–192 (2016).

[33]F. Zhu, N. Wang, R. Busch, and P. Haasen, "Ordering of the α-FeSi phase in a $Fe_{73.5}CuNb_3Si_{13.5}B_9$ magnet," Scr. Metall. Mater. **25**, 2011–2016 (1991).

[34]P. Allia, M. Baricco, P. Tiberto, and F. Vinai, "Kinetics of the amorphous-to-nanocrystalline transformation in $Fe_{73.5}Cu_1Nb_3Si_{13.5}B_9$," J. Appl. Phys. **74**, 3137–3143 (1993).

[35]T. Gheiratmand, H. R. Madaah-Hosseini, P. Davami, G. Ababei, and M. Song, "Mechanism of mechanically induced nanocrystallization of amorphous FINEMET ribbons during milling," Metall. Mater. Trans. A **46**, 2718–2725 (2015).

[36]T. Larimian, V. Chaudhary, M. U. F. Khan, R. V. Ramanujan, R. K. Gupta, and T. Borkar, "Spark plasma sintering of Fe–Si–B–Cu–Nb/Finemet based alloys," Intermetallics **129**, 107035 (2021).

[37]T. Gheiratmand, H. R. Madaah Hosseini, P. Davami, and C. Sarafidis, "Fabrication of FINEMET bulk alloy from amorphous powders by spark plasma sintering," Powder Technol. **289**, 163–168 (2016).

[38]R. Conteri, T. Borkar, S. Nag, D. Jaeger, X. Chen, R. V. Ramanujan, and R. Banerjee, "Laser additive processing of Fe-Si-B-Cu-Nb magnetic alloys," J. Manuf. Process. **29**, 175–181 (2017).

[39]T. Borkar, R. Conteri, X. Chen, R. V. Ramanujan, and R. Banerjee, "Laser additive processing of functionally graded Fe-Si-B-Cu-Nb soft magnetic materials," Mater. Manuf. Process. **32**, 1581–1587 (2017).

[40]T. Alam, T. Borkar, S. S. Joshi, S. Katakam, X. Chen, N. B. Dahotre, R. V. Ramanujan, and R. Banerjee, "Influence of niobium on laser de-vitrification of Fe–Si–B based amorphous magnetic alloys," J. Non-Cryst. Solids **428**, 75–81 (2015).

[41]Y. Yao, H. Huang, C. Chen, M. Ni, and S. Yang, "Effect of laser irradiation and tensile stress on microstructure and magnetic properties of Fe-based amorphous alloys," Nanomaterials **14**, 58 (2024).

[42]H. Wang, "Selective laser melting of Finemet soft magnetic material," MSc thesis, Virginia Polytechnic Institute and State University, 2023.

[43]I. Arganda-Carreras, V. Kaynig, C. Rueden, K. W. Eliceiri, J. Schindelin, A. Cardona, and H. S. Seung, "Trainable WEKA segmentation: A machine learning tool for microscopy pixel classification," Bioinformatics **33**, 2424–2426 (2017).

[44]R. B. Shah, M. A. Tawakkul, and M. A. Khan, "Comparative evaluation of flow for pharmaceutical powders and granules," AAPS PharmSciTech **9**, 250–258 (2008).

[45]M. Rodríguez-Sánchez, S. Sadanand, A. Ghavimi, R. Busch, I. Gallino, P. M. Tiberto, E. Ferrara, G. Barrera, L. Thorsson, H. J. Wachter, I. Gallino, and M. T. Pérez-Prado, "Relating laser powder bed fusion process parameters to (micro)structure and to soft magnetic behaviour in a Fe-based bulk metallic glass," Materialia **35**, 102111 (2024).

[46]G. Herzer, "Anisotropies in soft magnetic nanocrystalline alloys," J. Magn. Magn. Mater. **294**, 99–106 (2005).

[47]See supplementary material online for the processing conditions and properties of samples S1–S4 and R1–R6 that were manufactured to test the robustness of the experimental processing campaign (Supplementary Tables I and II) and the defect structure and the density of S1–S4 and R1–R6 specimens (Supplementary Figure 1).